Baroclinic Frontal Instabilities and Turbulent Mixing in the Surface Boundary Layer. Part I: Unforced Simulations

ERIC D. SKYLLINGSTAD AND R. M. SAMELSON

College of Earth, Ocean and Atmospheric Sciences, Oregon State University, Corvallis, Oregon

(Manuscript received 19 November 2010, in final form 6 April 2012)

ABSTRACT

Interaction between mixed layer baroclinic eddies and small-scale turbulence is studied using a nonhydrostatic large-eddy simulation (LES) model. Free, unforced flow evolution is considered, for a standard initialization consisting of an 80-m-deep mixed layer with a superposed warm filament and two frontal interfaces in geostrophic balance, on a model domain roughly 5 km × 10 km × 120 m, with an isotropic 3-m computational grid. Results from these unforced experiments suggest that shear generated in narrow frontal zones can support weak three-dimensional turbulence that is directly linked to the larger-scale baroclinic waves. Two separate but closely related issues are addressed: 1) the possible development of enhanced turbulent mixing associated with the baroclinic wave activity and 2) the existence of a downscale transfer of energy from the baroclinic wave scale to the turbulent dissipation scale. The simulations show enhanced turbulence associated with the baroclinic waves and enhanced turbulent heat flux across the isotherms of the imposed frontal boundary, relative to background levels. This turbulence develops on isolated small-scale frontal features that form as the result of frontogenetic processes operating on the baroclinic wave scale and not as the result of a continuous, inertial forward cascade through the intermediate scales. Analysis of the spectrally decomposed kinetic energy budget indicates that large-scale baroclinic eddy energy is directly transferred to small-scale turbulence, with weaker forcing at intermediate scales. For fronts with significant baroclinic wave activity, cross-frontal eddy fluxes computed from correlations of fluctuations from means along the large-scale frontal axis generally agreed with simple theoretical estimates.

1. Introduction

Most irreversible turbulent mixing in the ocean interior arises from small-scale instabilities driven by internal-wave shear (Henyey et al. 1986). An unknown additional fraction may also arise through downscale energy transfer from the approximately geostrophic mesoscale or submesoscale flow, despite classical theory that predicts a downscale cascade only of enstrophy (Charney 1971; Rhines 1977, 1979). In the surface boundary layer, small-scale baroclinic or frontal instabilities (Samelson 1993; Boccaletti et al. 2007), sometimes called ''mixed layer instabilities,'' may act to restratify the ocean boundary layer via primarily lateral motions. On the continuum from mesoscale motions to turbulence, these instabilities fill a niche between essentially balanced large-scale flows and the unbalanced circulations that lead directly to turbulent energy dissipation. They may arise when strong horizontal gradients with nearly vertical isopycnals form either from wind mixing or from straining by mesoscale eddies. The instability dynamics are essentially a gravitational slumping process, modified by rotation. Depending on the strength and lateral dimensions of the front, baroclinic eddies with horizontal scales between 1 and 10 km are rapidly produced, leading to strong lateral stirring on these scales in the mixed layer (for examples, see Boccaletti et al. 2007).

While simulations have provided basic descriptions of the dynamics of these small-scale baroclinic instabilities, we do not have a strong understanding of the processes that ultimately link these structures with three-dimensional turbulence, completing a downscale energy transfer from mesoscale circulations to dissipation. Hydrostatic primitive equation simulations have typically relied on lateral mixing via ad hoc diffusion [e.g., using a constant viscosity (Boccaletti et al. 2007; Fox-Kemper et al. 2008) or implicit numerical diffusion (Capet et al. 2008a,b; Molemaker et al.

Corresponding author address: Eric D. Skyllingstad, College of Earth, Ocean and Atmospheric Sciences, 104 CEOAS Admin. Bldg., Oregon State University, Corvallis, OR 97331-5503.
E-mail: skylling@coas.oregonstate.edu

DOI: 10.1175/JPO-D-10-05016.1

2010)] and are limited to scales of motion of $O(1\ \text{km})$ or larger. Capet et al. (2008a,b) and Molemaker et al. (2010) suggest that submesoscale eddies generate regions of large flow imbalance near finescale fronts. Instabilities in these regions are of $O(100\ \text{m})$ and are not resolved in the primitive equation simulations. Such simulations are thus unable to answer definitively questions concerning downscale mesoscale energy transfer, since small-scale instability processes are not resolved.

In this study, we simulate the interaction of small-scale baroclinic instabilities with turbulent mixing, bridging the scales between horizontally dominated submesoscale eddies and three-dimensional turbulence. Experiments are conducted using a nonhydrostatic large-eddy simulation (LES) model typically used to study ocean mixed layer processes such as Langmuir circulation and convective boundary layer growth. In the present case, the simulations are initialized with a double frontal system on which growing baroclinic waves develop along each front. We focus here on simulations without surface forcing, thereby isolating the effects of internal dynamical processes on the evolution of the flow.

Since turbulence production from surface forcing is frequently large in the surface boundary layer, the present simulations may be more generally representative of processes in the ocean interior. As scales contract, surface-forced mixed layer turbulent processes would begin to interact directly with these frontal circulations. For example, Langmuir circulations driven by wind and wave forcing often have scales on the order of 100 m (see, e.g., Thorpe 2004) and may have a direct influence on the evolution of these instabilities. Convective and shear-generated turbulence can also develop coherent structures that are similar in scale to the growing baroclinic waves and will likely affect the rate of mixing generated in frontal regions. It is likely that wind forcing will also affect instability development, possibly inhibiting or enhancing disturbance growth, depending on the orientation of the front relative to the wind direction. Analysis of an extended set of simulations with wind and wave forcing is in progress.

The paper is organized as follows: In section 2, the model is described along with initial conditions. In section 3, the simulations are briefly summarized. An analysis of small-scale turbulent fluxes in presented in section 4, and the energy budget is considered in section 5. A discussion and summary is presented in section 6.

2. Model and initial conditions

Very few simulations of frontal systems using nonhydrostatic, turbulence-resolving LES models have been conducted because of the large difference in scales between baroclinic waves and three-dimensional turbulent processes. LES models are also normally applied with periodic lateral boundary conditions, which require mean fields that are continuous across the domain. Although periodicity does not prevent inclusion of a mean background gradient, conditions similar to an open-ocean front are difficult to simulate without introducing the additional complexity of open boundary conditions. Here, we use a version of the standard, periodic ocean LES model described by Skyllingstad et al. (2000) and initialize a warm filament in the center of the model domain, thereby including frontal structure while avoiding the need for open lateral boundaries.

The LES model is based on the incompressible, nonhydrostatic, rotating *f*-plane, Boussinesq equations with subgrid turbulence parameterization following Ducros et al. (1996). Pressure is diagnosed using a conjugate-residual method described in Smolarkiewicz and Margolin (1994). The incorporation of the dynamically based parameterization of small-scale turbulence, which is coupled to the resolved velocity fluctuations at the large-scale end of the three-dimensional turbulent spectrum, and the inclusion of a nonhydrostatic vertical momentum balance are distinguishing features of this LES modeling approach. The Ducros et al. (1996) subgrid turbulence model is based on a Smagorinsky formulation, but with a variable Smagorinsky constant that depends on the local velocity structure function, so that the eddy viscosity and diffusivity at grid point (i, j, k) are defined as

$$\kappa_m = 0.0014 C_K^{-3/2} \Delta x [\tilde{F}(x, \Delta x, t)]^{1/2}, \quad \kappa_h = \kappa_m \mathrm{Pr}_t^{-1}, \quad (1)$$

where $C_K = 0.5$ is the Kolmogorov constant, $\mathrm{Pr}_t = 0.6$ is the turbulent Prandtl number, Δx is the grid spacing, and

$$\tilde{F}(x, \Delta x, t) = \frac{1}{4}(\|\tilde{u}_{i+1,j,k} - \tilde{u}_{i,j,k}\|^2 + \|\tilde{u}_{i-1,j,k} - \tilde{u}_{i,j,k}\|^2 + \|\tilde{u}_{i,j+1,k} - \tilde{u}_{i,j,k}\|^2 + \|\tilde{u}_{i,j-1,k} - \tilde{u}_{i,j,k}\|^2). \quad (2)$$

We note that (1) and (2) assume that the flow is isotropic and follows a Kolmogorov cascade. The three-component velocity field $\tilde{u}_{i,j,k}$ is computed using a discrete high-pass Laplacian filter to remove gradients produced by large-scale flow features. Consequently, energetic subgrid-scale mixing is only produced when large local velocity fluctuations arise in the resolved fields of motion.

The simulations presented here use a domain size of 5760 m in the alongfront direction, 10 500 m in the cross-front direction and a depth of 120 m with an isotropic grid

spacing of 3 m. To save computational time, experiments are initialized using a reduced grid with a resolution of 6 m until the frontal waves develop. Fields are then interpolated to the 3-m grid and used to conduct experiments for analysis.

For this study, we initialize two symmetric fronts using

$$T(x,z) = T_0(z) + \Delta T \tanh\left(\frac{2625 - x}{W}\right) \quad x < 5250 \text{ m} \quad \text{and} \quad (3)$$

$$T(x,z) = T_0(z) - \Delta T \tanh\left(\frac{x - 7875}{W}\right) \quad x > 5250 \text{ m},$$

where $T_0(z) = T_s$ for $z > -80$ m and $T_0(z) = T_s + 0.0241z$ for $z > -80$ m, $\Delta T = 0.04$°C, $W = 600$ m, z is depth (m), and x is the cross-frontal coordinate ranging from 0 to 10 500 m. The Coriolis parameter $f = 1.4 \times 10^{-4}$ s^{-1}, and an initial state with pressure and velocity in hydrostatic and geostrophic balance is prescribed, with no flow at the bottom. To provide a small perturbation to this initial balanced state, a weak surface heat flux of -10 W m^{-2} with a 1 W m^{-2} random spatial variation is applied for 8 h. After 12 h, the front has developed a slight slope from initial adjustment processes and has gradually widened from numerical and parameterized dispersion generated by the initial random heating, but it has not yet generated finite-amplitude, large-scale disturbances (Fig. 1).

The space and time scales for the fastest-growing waves that develop on the unstable front can be estimated following Stone (1966) as

$$L_s = \frac{2\pi}{k_s} = \frac{2\pi U}{f}\sqrt{\frac{1 + \text{Ri}}{5/2}} \quad \text{and} \quad (4)$$

$$\tau_s(k_s) = \sqrt{\frac{54}{5}}\sqrt{\frac{1 + \text{Ri}}{f}}, \quad (5)$$

respectively, where L_s is wavelength, k_s is wavenumber, and τ_s is an e-folding time (e.g., Fox-Kemper et al. 2008). Here $U = (-H/f)(\partial B/\partial x)$ is the geostrophic velocity scale, H is the mixed layer depth, f is the Coriolis term, $\text{Ri} = N^2 f^2/(\partial B/\partial x)^2$ is the mean balanced Richardson number with Brunt–Väisälä frequency $N^2 = -(g/\rho)(\partial\rho/\partial z)$, $B = -g(\rho'/\rho_o)$ is the buoyancy, $\rho_o = 1025$ kg m^{-3} is the background seawater density, and g is gravitational acceleration. Density variations are defined as a linear function of temperature, $\rho'/\rho_o = \alpha T'$, where $\alpha = -2 \times 10^{-4}$ K^{-1} is the thermal expansion coefficient. According to (4) and (5), the temperature field (3) should generate growing baroclinic waves with

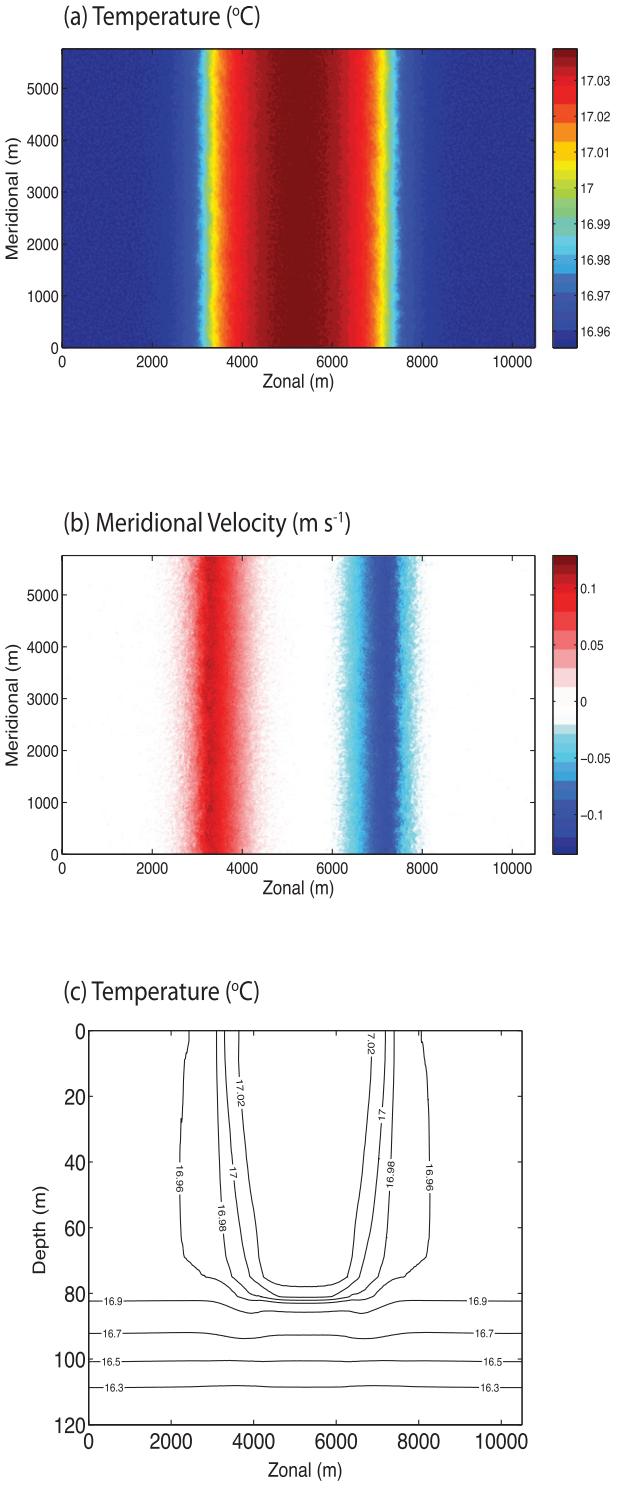

FIG. 1. Horizontal sections of (a) surface temperature, (b) surface meridional velocities, and (c) a vertical cross section of temperature from hour 12.

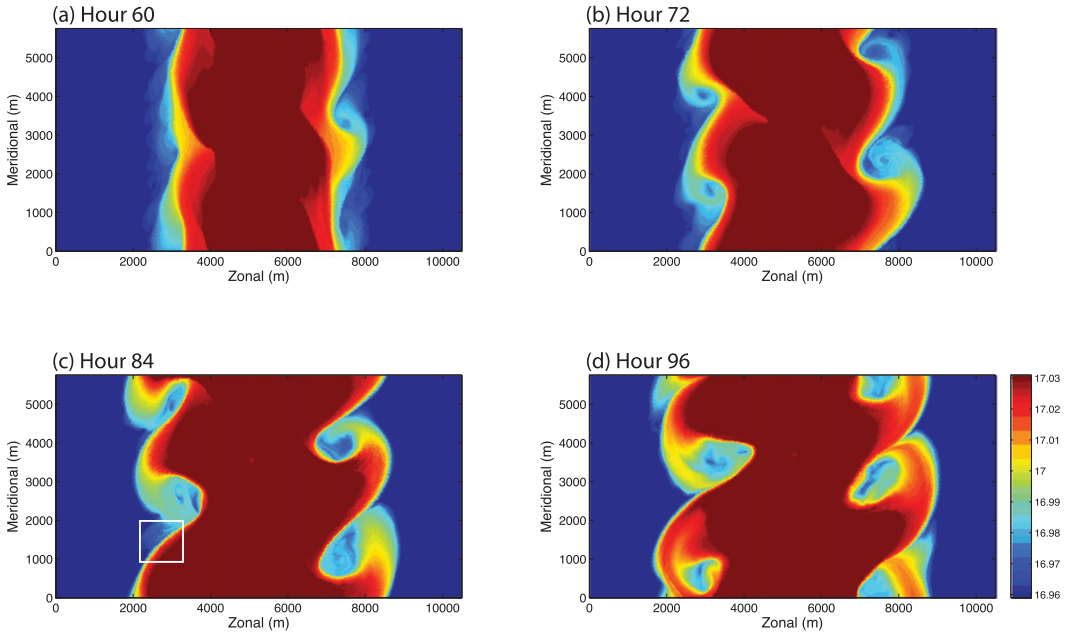

FIG. 2. Horizontal sections of temperature (°C) taken at hours (a) 60, (b) 72, (c) 84, and (d) 96 from a depth of 4.5 m for the unforced case simulation. The box indicates the subdomain plotted in Fig. 4.

time and space scales on order of $\tau_s \approx 9$ h and $L_s \approx 4$ km, and we consider the evolution of the flow over 96 h.

3. Flow evolution

a. Baroclinic waves

The small perturbations introduced into the unstable geostrophic initial flow during the first eight hours develop into finite-amplitude baroclinic waves on each front within 2 days. Both fronts begin to meander at around hour 60 with two major waves on each front (Figs. 2, 3). By hour 96, waves on both fronts evolve into closed circulations with smaller, detached cold eddies forming and transporting water into the warm region. Both frontal systems develop baroclinic waves over a similar time period; however, there is a slight delay in the development on the left side ($x < 5000$ m) front. Overall, the frontal structure is markedly deformed but does not show evidence of significant irreversible cross-frontal mixing except near the baroclinic eddy structures. In fact, many sections of the front sharpen over time in response to baroclinic instability: for example, near $x = 2500$ m, $y = 1000$ m at hour 84 or near $x = 7000$ m, $y = 1000$ m at hour 96. As the frontal gradients change, the meridional velocity follows suit in approximate geostrophic balance with the changing thermal wind gradient (Fig. 3). For example, the maximum southward velocity at hour 96 is located near the sharpened front noted above.

b. Turbulence

The dominant horizontal scales of the horizontal velocity field are those of the developing baroclinic waves (Fig. 3). The horizontal structure of the vertical velocity field is dominated instead by much smaller scales, with the largest vertical velocities of both signs occurring in the narrow regions of intensified lateral temperature and velocity gradients, where the cross-frontal scales have collapsed so that the initial cross-frontal temperature and velocity differences of 0.1°C and 5–10 cm s^{-1} occur over a distance on the order of 100 m (Fig. 4). These large vertical velocities are associated with resolved, small-scale turbulent fluctuations that arise from small-scale instabilities on the locally intensified frontal velocity gradients. Disturbances with scales on the order of 10–50 m are centered along the front in the region with highest horizontal shear. The associated velocity fluctuations are roughly isotropic, with amplitudes of several centimeters per second (Figs. 4a,c).

The structure of the flow field thus indicates the existence of enhanced small-scale turbulence that is associated with the baroclinic wave activity. However, this enhanced turbulence is not distributed homogeneously throughout the baroclinic wave field. Instead, it is concentrated at the order 100-m-width frontal features that have arisen from frontogenetic forcing by the large-scale field. In these highly localized regions, the turbulence develops spontaneously through small-scale instability of the intense lateral shear flows. The frontogenesis is

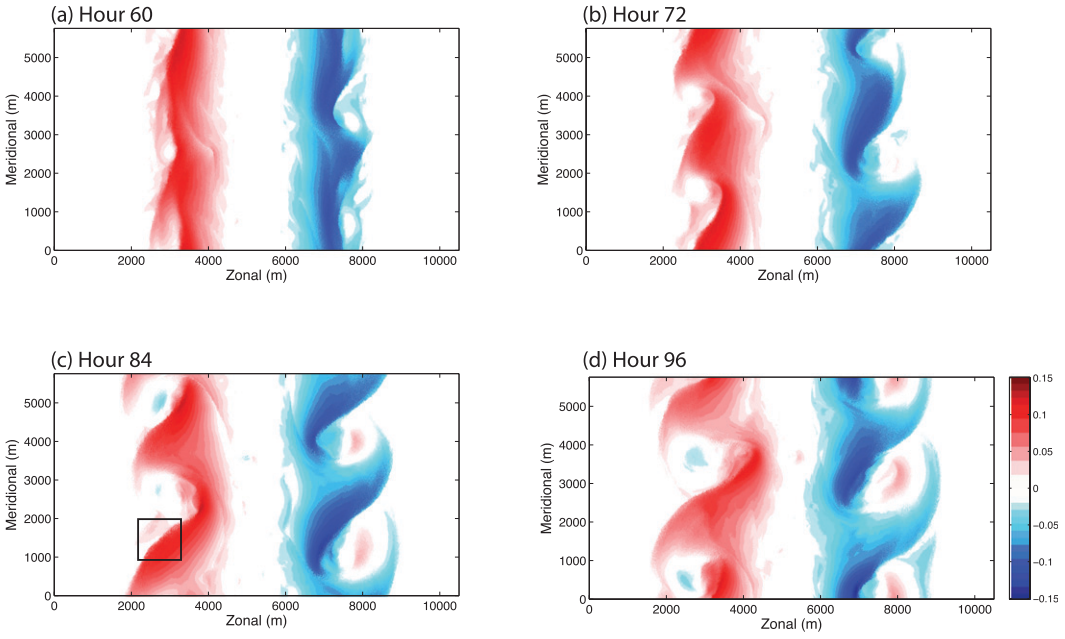

FIG. 3. As in Fig. 2, but for meridional velocity (m s^{-1}).

a natural consequence of baroclinic instability as frontal boundaries are strained by wave-induced circulations and develop ageostrophic secondary circulations (e.g., Hoskins and Bretherton 1972). Thus, it is clear already from the structure of the physical fields that the baroclinic modes evidently do not trigger a turbulent forward cascade of energy through a continuous range of spatial scales toward the dissipation range. Instead, a spectrally nonlocal downscale transfer of energy occurs, with small-scale structures arising directly through instabilities of the intensified frontal features, which otherwise appear essentially laminar over the intermediate range of scales from 100 m to several kilometers.

c. *Departure from balance*

Typically, small-scale velocity perturbations can be anticipated to arise when three-dimensional nonlinear terms in the divergence equation are of the same order as the horizontal pressure $(1/\rho)\nabla_h^2 p$, Coriolis $f\zeta^z$, and curvature $\nabla \cdot (u_h \nabla_h u_h)$ terms; here, ρ is the density, p is the pressure, f is the Coriolis parameter, ζ^z is the vertical component of vorticity, u_h is the horizontal velocity, and subscript h implies horizontal gradients. An associated balance parameter can be defined as

$$\varepsilon_{\text{bal}} = \frac{\left|\nabla \cdot (u_h \cdot \nabla_h u_h) - f\zeta^z + \frac{1}{\rho}\nabla_h^2 p\right|}{|\nabla \cdot (u_h \cdot \nabla_h u_h)| + f|\zeta^z| + \left|\frac{1}{\rho}\nabla_h^2 p\right| + \mu}, \quad (6)$$

where $\mu = f\zeta^z_{\text{rms}} + |(1/\rho)\nabla_h^2 p\,|_{\text{rms}}$ is added to avoid the appearance of strong imbalance in regions of the flow where circulations are weak (Capet et al. 2008b). Values of ε_{bal} near zero indicate flow that is in a geostrophic or gradient-wind balance, whereas, as ε_{bal} approaches 1, circulations are strongly unbalanced with vertical circulations that are similar in scale to horizontal perturbations. In the present simulations, small-scale velocity structures are primarily evident along the front and produce values of ε_{bal} systematically near 1 (Figs. 4a,d). Note that the order 1 cm s^{-1} vertical velocities associated with these disturbances are at the low end of velocity scales for typical turbulence found in the wind-forced ocean mixed layer. Consequently, this process is likely to be of most significance away from energetic boundary layer turbulence or during periods of weak or no wind forcing.

4. Small-scale turbulent fluxes

The simulations described above span the full range of scales between the weakly unstable baroclinic fronts with growing, near-geostrophic waves, and the large-eddy motions of three-dimensional, ageostrophic, nonhydrostatic turbulent microstructure resolved by the LES approach. Irreversible small-scale turbulent mixing in the model is accomplished by subgrid-scale diffusion, in which the magnitudes of the turbulent diffusivities are computed from the local amplitude of the resolved large-eddy motions using the closure scheme (1) and (2) so that the

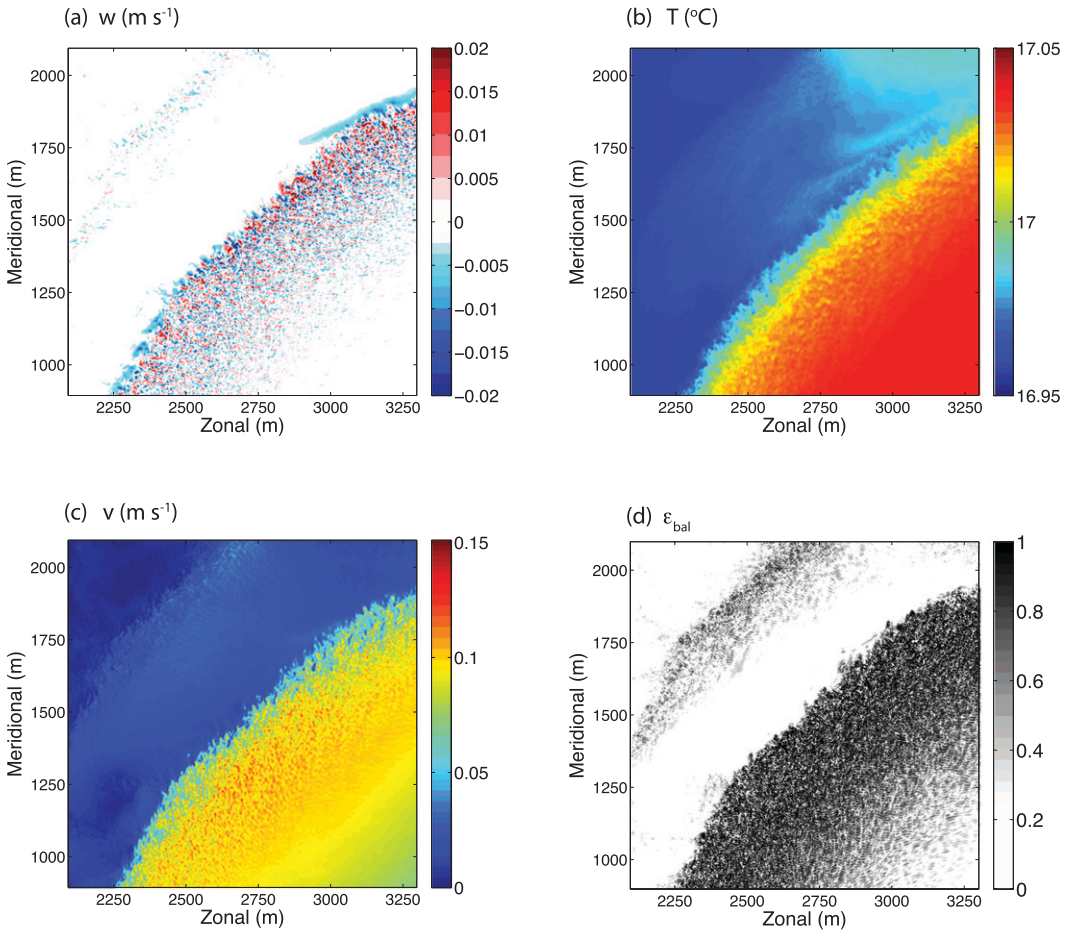

FIG. 4. Subsection plots of (a) vertical velocity w at 6-m depth, (b) temperature, (c) meridional velocity v, and (d) flow balance parameter (see text for definition) from 4.5-m depth. Plots are from hour 84 (shown as box inset in Figs. 2, 3). Close inspection shows that finescale disturbances are resolved by roughly 8–10 grid points.

resolved turbulence controls the local mixing rates in a dynamically consistent manner. Consequently, it is possible to ask directly whether there are correlations between the geostrophic wave structures on the large scale and the irreversible turbulent fluxes on the small scale. Such correlations would also be evidence of a direct downscale transfer of energy, in which large-scale, near-geostrophic motions cause small-scale turbulence and energy dissipation. This downscale energy transfer, if indeed it exists at all, is anticipated to be weak, because of the conservative properties of near-geostrophic flow and the weak coupling of geostrophic and ageostrophic motions.

Here, the connection between baroclinic wave and turbulent activities is analyzed by directly examining quantities associated with subgrid-scale turbulent fluxes. First, distributions of subgrid-scale turbulent heat diffusivity κ_h [(1)] are computed to determine whether there are elevated turbulent diffusivities associated with the baroclinic wave activity. Second, internal diabatic heat fluxes are computed from these diffusivities and the temperature field to determine whether the anomalous diffusivities cause anomalous fluxes. Third, an attempt is made to diagnose volumes and volume changes in isothermal classes to compare to volume changes estimated from the computed diabatic fluxes.

Frequency distributions of the LES-closure turbulent-microstructure thermal diffusivity κ_h show that there are roughly 10 times more grid points with large diffusivities at hour 84, after the development of baroclinic waves, than at hour 48, prior to the growth of large-scale disturbances (Figs. 5a,b). The distributions peak at background diffusivity values on the order of $10^{-6} - 10^{-5}$ m^2 s^{-1}, roughly consistent with existing estimates and observations of ocean-interior turbulent diffusivity distributions. The large values of model κ_h are systematically associated with frontal structures in the baroclinic waves (Figs. 5c,d). Thus, there is enhanced microstructure turbulence

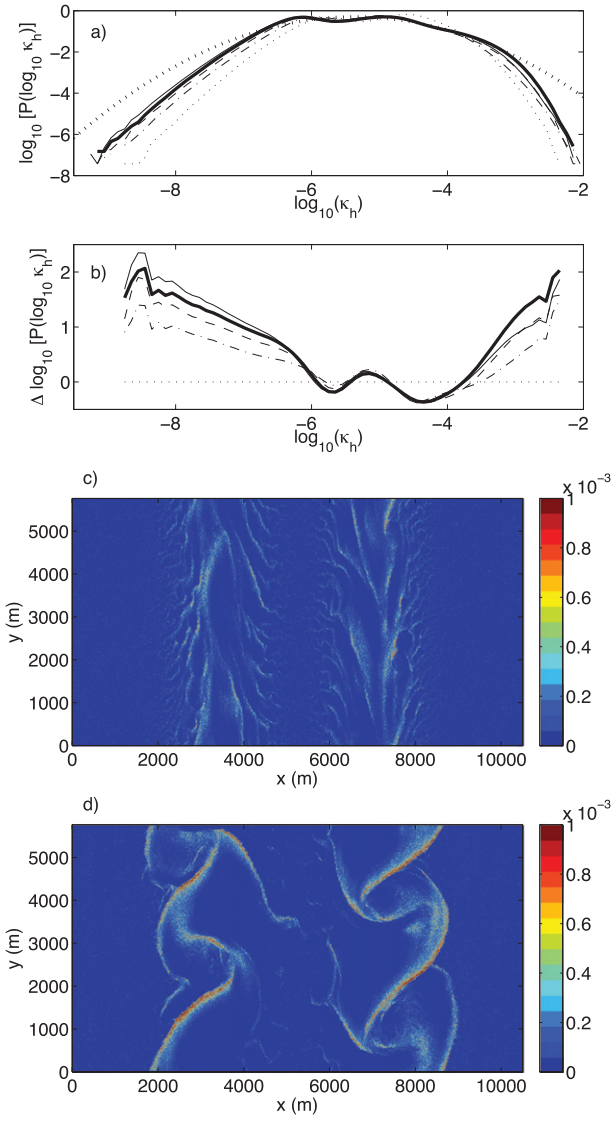

FIG. 5. (a) Probability distributions $P(k_h)$ of κ_h (m^2 s^{-1}) at hours 48 (dotted), 60 (dashed–dotted), 72 (dashed), 84 (thick solid), and 96 (thin solid). A normal distribution with the same mean and variance as for hour 84 is also shown (transverse dashes). (b) Differences of $\log_{10}$ of respective probability distributions from the hour-48 distribution. Contours of surface κ_h (m^2 s^{-1}) vs x and y (3-m grid indices) at hours (c) 48 and (d) 84.

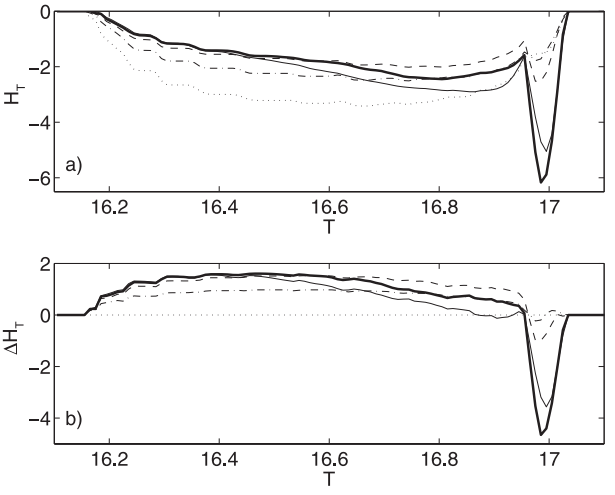

FIG. 6. (a) Area-integrated subgrid-scale turbulent diffusive heat (temperature) fluxes H_T (°C m^3 s^{-1}) through isothermal surfaces 16.1°C < T < 17.1°C at hours 48 (dotted), 60 (dashed–dotted), 72 (dashed), 84 (thick solid), and 96 (thin solid). Here, H_T is computed as the integral of the differential flux $dH_T = -\kappa_h \nabla T \cdot \mathbf{n} dA_T$ over the area A_T of the T-isothermal surface. (b) Differences of corresponding fluxes from hour-48 values.

associated with baroclinic wave activity in the LES simulations. These enhanced subgrid-scale diffusivities arise from enhanced small-scale resolved velocity fluctuations in the corresponding regions of the flow. This is direct evidence for the existence of a downscale transfer of energy, in which large-scale near-geostrophic motions induce small-scale turbulence in localized regions.

In addition to the enhanced turbulent diffusivities, there are significant increases in the magnitude of integrated turbulent diffusive heat (temperature) flux H_T across isothermal surfaces in the frontal range 16.95°C < T < 17.05°C during hours 60 through 92 relative to hour 48 (Fig. 6). The flux H_T was computed as the integral of the differential flux $dH_T = -\kappa_h \nabla T \cdot \mathbf{n} dA_T$ over the area A_T of the T-isothermal surface, where the normal $\mathbf{n} = \nabla T/|\nabla T|$, so that the flux is negative when the diffusivity is positive. There is also a systematic decrease during this period in the magnitudes of the corresponding fluxes across isothermal surfaces in the thermocline range, 16.1°C < T < 16.9°C (Fig. 6). The magnitude of the thermocline-range fluxes generally remains constant or decreases monotonically but at a decreasing rate during hours 72 through 96, while the magnitude of the frontal-range fluxes reaches a maximum near hour 84 and then declines at hour 96 (Fig. 6). These changes may arise from variations in local values of the turbulent diffusivities as indicated in the κ_h distributions (Fig. 5), in the total area of the resolved isothermal surfaces, or in the resolved thermal gradients across isothermal surfaces.

The area of isothermal surfaces in the thermocline range is essentially constant during hours 48 through 96, except for a decrease in area of the coldest surfaces, associated with warming of the deepest fluid by diffusive flux convergence adjacent to the insulated bottom boundary (Fig. 7). In the thermocline range, the isothermal surface areas increase monotonically over this period, as the front is distorted by the baroclinic waves. The maximum increase in thermocline-range isothermal surface area is 50%, a significant increase but too small to account alone for the tripling of the integrated heat flux in this range

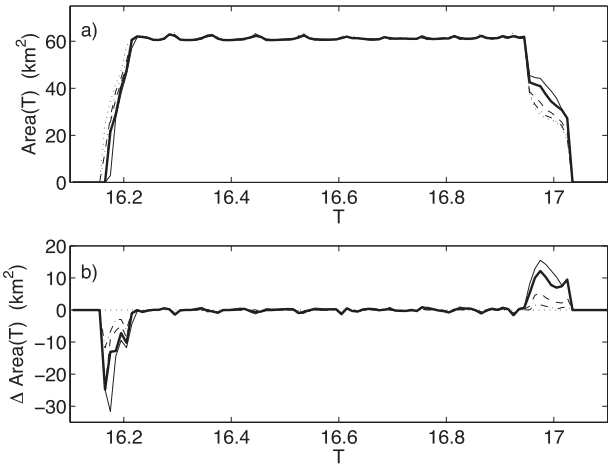

FIG. 7. (a) Area A_T (km^2) of isothermal surfaces with temperature T at hours 48 (dotted), 60 (dashed–dotted), 72 (dashed), 84 (thick solid), and 96 (thin solid). Areas are computed for surfaces that follow the cell faces of the computational grid. Undulations in the thermocline-range (16.1°C $< T <$ 16.9°C) areas arise from the latter area definition and the finite vertical grid size, which together produce abrupt changes in vertical cell-face areas when nearly horizontal isothermal surfaces depart sufficiently from horizontal planes. (b) Differences of corresponding isothermal surface areas from hour-48 area.

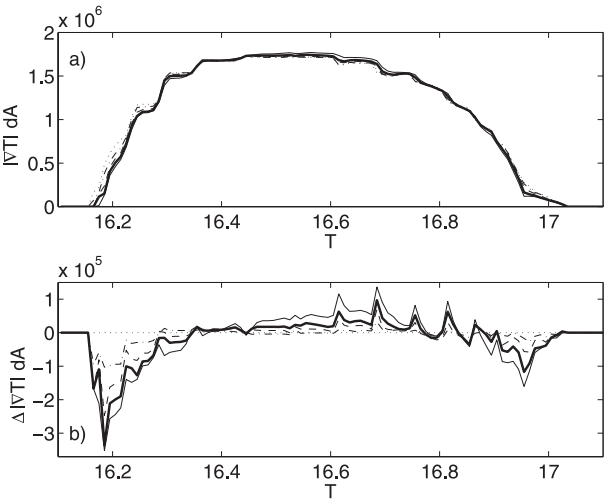

FIG. 8. (a) Integrals over isothermal surfaces of the sum of the absolute values of the three Cartesian components of $\nabla T \cdot \mathbf{n} dA_T$ (°C m) at hours 48 (dotted), 60 (dashed–dotted), 72 (dashed), 84 (thick solid), and 96 (thin solid). Areas are computed as in Fig. 7. (b) Difference of corresponding area means from hour-48 values.

(Fig. 6). In addition, the thermocline-range surface area continues to increase at hour 96, when the heat flux has begun to decrease (Fig. 6). Thus, the increased flux in the thermocline range cannot be ascribed to the changes in resolved area of the isothermal surfaces. Of course, the enhanced irreversible subgrid-scale diffusivities κ_h themselves effectively represent increased isothermal surface area at the molecular-diffusive scale, so that the associated increased irreversible fluxes can ultimately also be interpreted as the result of surface area changes. The distinction made here is between the effect of the baroclinic wave activity on the large-scale isothermal surface areas and on the local microstructure turbulent diffusivities or their molecular-diffusive area equivalents. Both of these effects contribute to the enhanced flux, but the former is not sufficient to explain it, suggesting in turn that locally enhanced microstructure fluxes must also contribute.

For fixed isothermal surface area, enhanced subgrid-scale fluxes can be produced either from an increase in the diffusivity κ_h or from an increase in the temperature gradient $|\nabla T|$. Integrals of the latter over the isothermal surfaces, computed as the sum of the absolute values of the three Cartesian components of $\nabla T \cdot \mathbf{n} dA_T$ over the computational grid, show that the effective area-mean $|\nabla T|$ decreases slightly in the frontal range during hours 48 through 96 (Fig. 8). Thus, the increased flux in the frontal range cannot be ascribed to increases in the temperature gradient.

Consequently, the local increase of the turbulent diffusivities κ_h associated with the baroclinic wave activity in the frontal zones (Fig. 5) evidently contributes essentially to the increased heat fluxes through isothermal surfaces (Fig. 6). Consistent with the spatial correlation of large surface κ_h values with the distorted surface frontal features at hour 84 (Fig. 5), all of the large values and large changes in isothermal-surface area-mean κ_h occur in the frontal range 16.95°C $< T <$ 17.05°C (Fig. 9). This

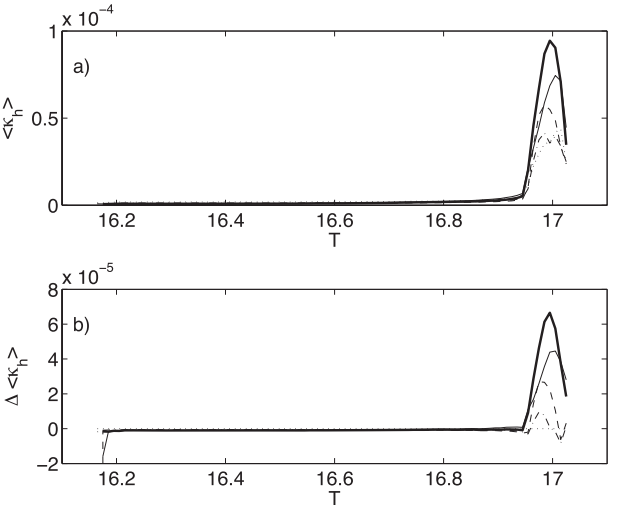

FIG. 9. (a) Isothermal-surface area-mean κ_h (m^2 s^{-1}) at hours 48 (dotted), 60 (dashed–dotted), 72 (dashed), 84 (thick solid), and 96 (thin solid) for isothermal surface areas computed as in Fig. 7. (b) Difference of corresponding area means from hour-48 values.

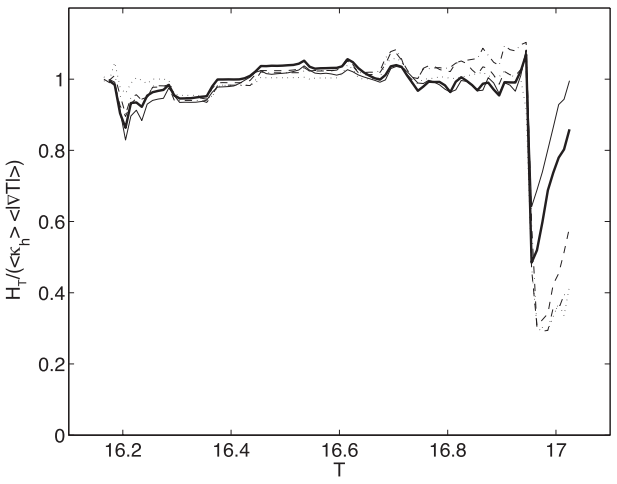

FIG. 10. Effective correlation of κ_h with $|\nabla T|$ on isothermal surfaces, computed as the magnitude of the ratio of the area-mean heat flux (from Fig. 6, divided by isothermal surface area) to the product of the respective area means of κ_h and $|\nabla T|$, at hours 48 (dotted), 60 (dashed–dotted), 72 (dashed), 84 (thick solid), and 96 (thin solid), for isothermal surface areas computed as in Fig. 7.

is direct evidence of a downscale transfer of energy: the large-scale, near-geostrophic, baroclinic waves cause local elevations in the level of microstructure turbulent kinetic energy and enhanced local irreversible fluxes arising from the locally elevated turbulent activity. The area-mean κ_h in the frontal temperature range roughly doubles from hour 48 to hour 84 and then declines from hour 84 to hour 96, consistent with the doubling and subsequent decline of the corresponding fluxes (Fig. 6). Because isothermal surface areas in the frontal range also increase during this period (Fig. 7), the effective correlation of κ_h with $|\nabla T|$ on isothermal surfaces must be less than one, in order that the net flux increase not exceed the diagnosed doubling. This is indeed the case: this correlation, computed as the magnitude of the ratio of the area-mean heat flux to the product of the respective area means of κ_h and $|\nabla T|$, is near one throughout the thermocline range but is generally between 0.3 and 0.8 in the frontal range (Fig. 10). Thus, roughly half of the small-scale turbulence induced by the baroclinic wave activity develops in regions of relatively small temperature gradient that are embedded in the frontal zones. Because $|\nabla T|$ is dominated by its vertical component, this is consistent with standard ideas regarding stratified turbulence, which indicate that, as velocity shear increases, the onset of turbulence will occur first in the regions of weakest stratification.

The area-integrated heat flux through isothermal surfaces (Fig. 6) can be differentiated with respect to temperature to obtain a rate of change of volumes of isothermal classes of fluid. For example, the increasing negative flux from $T = 17.05$°C to $T = 17$°C indicates a net removal of heat from the volume of fluid with $17°C < T < 17.05°C$ and a conversion of some of this fluid to a cooler isothermal class. In principle, it should be possible to compute these conversions independently from the model fields, by comparing the instantaneous volumes of the corresponding isothermal classes at different times. However, efforts to diagnose these changes failed, as the implied volume differences proved to be too small to be resolved by the model grid. This is in part both a consequence and a measure of the relative weakness of the downscale transfer of energy: although the changes in model diffusivity and heat flux can be reliably diagnosed, the resulting absolute changes in isothermal volume classes over the 96-h simulation are too small to compute directly.

The subgrid-scale parameterization scheme, by which κ_h is computed from the resolved small-scale velocity fluctuations, is based on the classical concept of a downscale, or forward, turbulent cascade (e.g., Tennekes and Lumley 1972; Frisch 1995): it is presumed that energy that is in the turbulent field near the grid scale cascades successively to smaller scales through an inertial range, in which nonlinear interactions that are local in wavenumber space and approximately isotropic in physical space cause a flux of turbulent energy toward smaller scales through a continuous range of wavenumbers that extends to the dissipation scale. In the present context, in which large-scale baroclinic waves have been shown to be a source of enhanced small-scale turbulent activity, it is natural to ask whether the energy transfer from the baroclinic wave scale to the small scale can also be characterized as a cascade. As anticipated from the velocity structure analysis in section 3, it seems clear from the spatial structure of the enhanced diffusivities (Fig. 5) that this is not the case. Rather than arising as a statistically uniformly distributed field as in a quasi-isotropic turbulent cascade, the enhanced diffusivities are associated with resolved transitions to turbulent motion that occur in highly localized, anisotropic, frontal features with large velocity shears and temperature gradients (Fig. 5). The development of these frontal features is a coherent, quasi-laminar, spectrally nonlocal process, in which the baroclinic wave scales of the flow effectively collapse directly toward the 100-m cross-frontal scales, rather than through a continuous turbulent cascade. Consequently, we believe that it is not correct to refer to the inferred downscale transfer of energy from the baroclinic waves to the small-scale turbulent fluctuations as a downscale, or forward, cascade: the transfer is not a cascade in the classical sense, with the dominant interactions being local in wavenumber space, but is instead mediated by frontogenetic large-scale processes, which are strongly nonlocal in wavenumber and

are associated with an abrupt, essentially laminar collapse of scales through the intermediate range. This collapse supports the development of localized, coherent, frontal features with large thermal and velocity gradients, on which turbulence then develops through local instability processes and shear-driven transitions on scales on the order of 10–100 m that are resolved by the LES model.

5. Energy budget

Analysis of the kinetic energy budget provides a third perspective on the transfer of energy across scales in the model. We first examine the time evolution of the perturbation kinetic energy $K' = 0.5u_i'^2$ by calculating the averaged budget,

$$\frac{\partial K'}{\partial t} = u_i' \cdot \frac{\partial u_i}{\partial t} = -u_i' u_j \frac{\partial u_i}{\partial x_j} - u_i' \frac{\partial p}{\partial x_i} - u_3' \delta_{i3} g \frac{\rho'}{\rho_o} - u_i' \cdot \frac{\partial (\overline{u_i'' u_j''})}{\partial x_j} \quad (7)$$

where

$$u_i'(x,y,z,t) = u_i(x,y,z,t) - U_i(x,z,t),$$

$$U_i(x,z,t) = \frac{1}{y_{\max}} \sum_{y=0}^{y=y_{\max}} u_i(x,y,z,t)\Delta y, \quad \text{and}$$

$$\overline{u_i'' u_j''} = -\kappa_m \frac{\partial u_i}{\partial x_j},$$

and then computing the domain average. The terms in (4) are referred to here as storage (term I), energy flux divergence (term II), pressure work (term III), buoyancy production (term IV), and dissipation (term V). Average velocity fields U_i are calculated as meridional means and approximately represent the geostrophic background flow that is initially in thermal wind balance. Since the meridional mean of the perturbation velocity vanishes, the full-domain integral of term I in (7) is then equal to the rate of change of the domain integral of the fluctuation kinetic energy. We note that the advective transport of K' averages to zero in term II because of closed boundary conditions; hence, this term can also be thought of as a shear production.

Energy production in the model is dominated by the buoyancy term IV, representing the release of available potential energy from the horizontal density gradients of the large-scale flow (Fig. 11). The positive storage term I

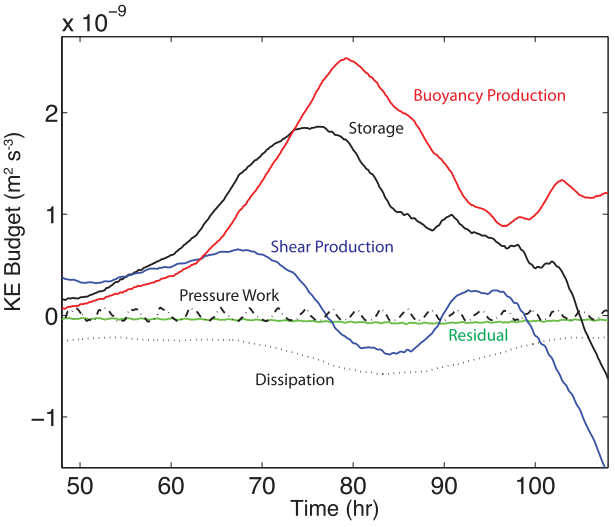

FIG. 11. Domain volume-averaged kinetic energy budget terms as a function of time. Terms represent the domain volume averages of the corresponding quantities I–V in (7), as defined in the text. The residual term is defined as term I minus the sum of terms II, III, IV, and V.

represents the increasing kinetic energy of the growing baroclinic waves. The energy flux divergence term II represents conversion of mean kinetic energy associated with the nominally geostrophic background flow to perturbation kinetic energy contained in baroclinic waves and turbulence. Initially, terms II and IV are both positive, indicating that the instability is of mixed baroclinic–barotropic type. As the disturbances amplify, this term reverses sign, suppressing the wave growth as the waves occlude around hour 78 (Fig. 2), after which time wave growth decreases rapidly with formation of ring circulations by hour 96. This transition reflects the classical progression of a baroclinic life cycle from baroclinic, or mixed baroclinic–barotropic, growth to barotropic decay (e.g., Simmons and Hoskins 1978; Samelson and Chapman 1995). The dissipation term is always removing energy but during most of the simulation is much smaller than the buoyancy forcing. The pressure work term (term III) has a small oscillation associated with pseudocompressibility of the iterative numerical solver; when averaged over the oscillation period, this term is negligibly small, as required for an unforced incompressible fluid in a periodic domain with a rigid top and bottom.

Vertical profiles of horizontal averages of the instantaneous balance (7) at hour 72 show that the buoyancy production (term IV) is a large generation term through the middle of the mixed layer, with the energy flux divergence term (term II) adding energy except near the surface and near the mixed layer bottom (Fig. 12). Dissipation is relatively weak throughout the entire column with a

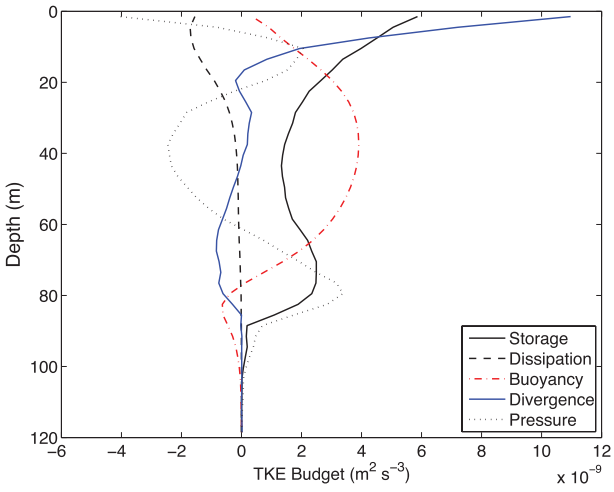

FIG. 12. Horizontally averaged kinetic energy budget terms as described in the text. Plot is averaged over 30 min, starting at hour 72.

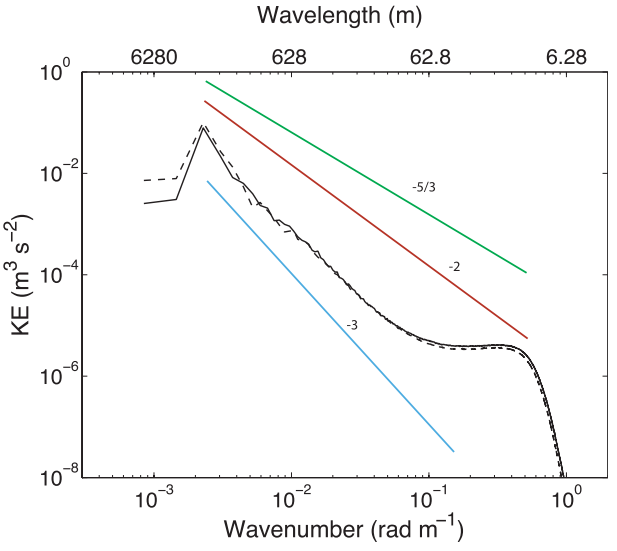

FIG. 13. Two-dimensional KE spectra calculated as described in the text. The solid line is from hour 84, and the dashed line is from hour 96. Colored lines denote various spectral slopes as labeled.

maximum near the surface where small-scale eddies have the largest amplitude (e.g., Fig. 4). Pressure work primarily acts to redistribute energy away from the middle of the mixed layer and counteracts shear production near the surface. Worth noting is the similarity of the buoyancy production vertical structure to estimated buoyancy flux from linear theory (Stone 1972) presented in Fox-Kemper et al. (2008), indicating that much of this term is related to baroclinic instability rather than turbulent mixing.

A key question in our analysis concerns the fate of kinetic energy generated at baroclinic scales, which can be removed from the system either by a gradual cascade of energy through progressively smaller-scale, quasi-two-dimensional eddies or through direct production along frontal boundaries of three-dimensional turbulence that decays via subgrid-scale viscous dissipation. The structure of kinetic energy spectra as a function of horizontal wavenumber magnitude $k = \sqrt{k_x^2 + k_y^2}$ for the current simulation (from a two-dimensional spectral decomposition, averaged over wavenumber vectors of approximately equal magnitude, and then divided by k to obtain the spectral density) also suggests that energy at large scales is not removed by a continuous inertial cascade process: the spectral slope is about -3, more indicative of an energy-conserving enstrophy cascade than an energy-cascade regime, and there is enhanced energy and a nearly flat spectrum at the largest wavenumbers, between scales of 6 and 60 m (Fig. 13). A rough estimate of the dissipation spectra may be obtained by multiplying the kinetic energy spectra (Fig. 13) by k^2, suggesting a modest peak at larger wavenumbers $k > 0.1$ m^{-1}; the corresponding variance-preserving form, obtained by multiplying by a third factor of k, would indicate that the dominant contribution to the integrated dissipation is from wavenumbers $k > 0.1$ m^{-1} or at scales smaller than 60 m but still well resolved by the 3-m grid spacing.

A more complete description of the spectral scale interactions can be obtained through a spectral decomposition of the kinetic energy balance (Frisch 1995; Capet et al. 2008c; Molemaker et al. 2010),

$$\widehat{u_i'}^* \cdot \frac{\partial \widehat{u_i'}}{\partial t} = \widehat{u_i'}^* \cdot \widehat{u_j \frac{\partial u_i}{\partial x_j}} - \widehat{u_i'}^* \cdot \frac{\partial \widehat{p}}{\partial x_i} - \widehat{u_3'}^* \widehat{\delta_{i3} g \frac{\rho'}{\rho_o}} - \widehat{u_i'}^* \cdot \frac{\partial \widehat{(\overline{u_i'' u_j''})}}{\partial x_i}, \tag{8}$$

where $\hat{u}(k_x, k_y, z)$ denotes a two-dimensional spectral transform in the horizontal direction, the asterisk denotes complex conjugate, and terms are otherwise defined as in (7). For this analysis, the perturbation velocity and the terms that enter in (8) from the right-hand side of the momentum balance were computed and integrated vertically over the entire model domain and separately averaged temporally over a 5-min time period, with the product then providing snapshots of the spectral energy balance at two different model times, hours 84 and 96, representing peak wave growth and reduced growth with established ring or eddy circulation features, respectively (Fig. 14). The storage term in (8) was calculated by computing the difference in spectral energy over the 5-min averaging period and used to estimate the budget residual (Fig. 14).

The integrated spectral fluxes,

$$\Pi(k) = \int_k^{k_{\max}} \phi(k)\, dk, \tag{9}$$

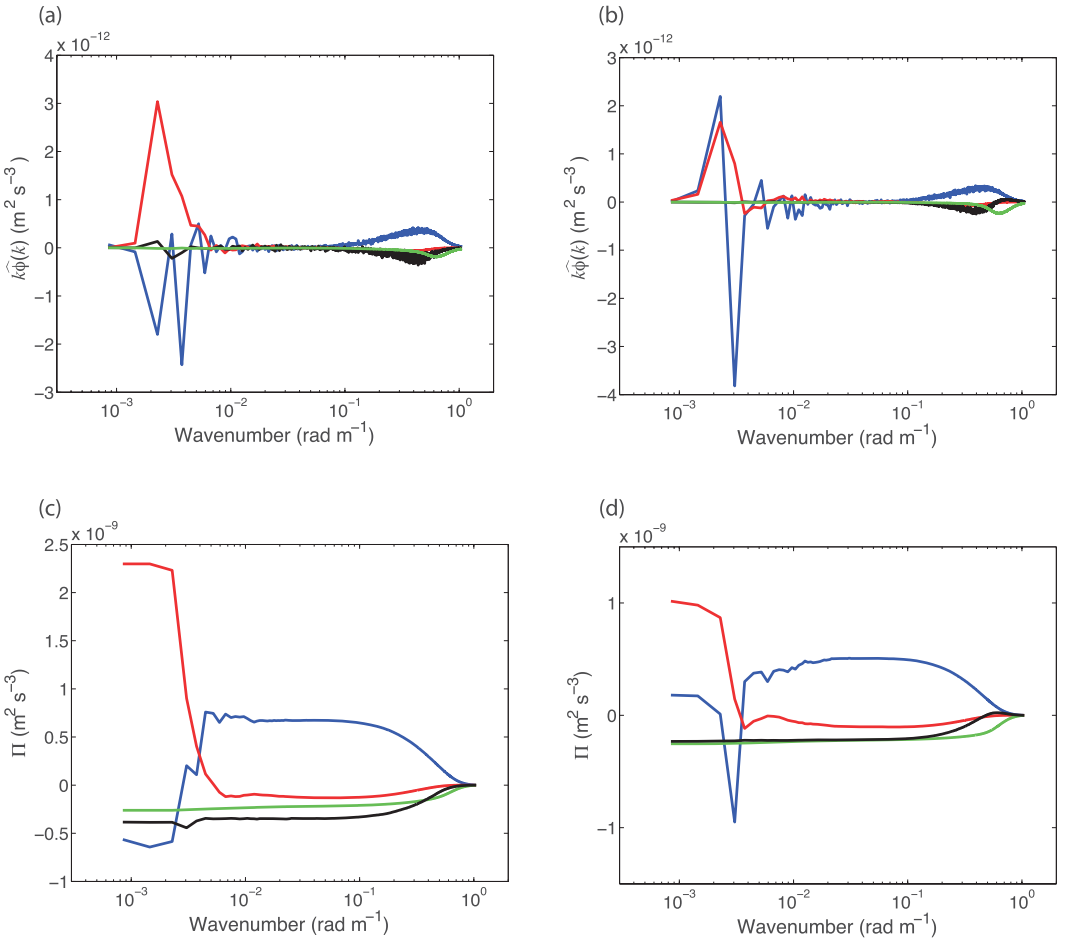

FIG. 14. Domain averaged spectral components of the (a),(b) kinetic energy budget and (c),(d) spectral energy flux for hours (a),(c) 84 and (b),(d) 96. The energy flux divergence term is blue, the buoyancy term is red, the dissipation term is green, and the residual is black. Spectral components in (a),(b) are multiplied by wavenumber k to preserve variance.

where $\varphi(k)$ are the individual terms in (8), provide a measure of the direction of energy transfer by each term in the budget. For example, positive values for the integrated energy flux divergence term indicate a forward transport for larger wavenumbers, with energy removed by dissipation and numerical effects at small scales (Fig. 14). The relatively constant values for the dissipation and residual for $k < 0.1$ m^{-1} indicate that energy loss from these terms occurs only at the small scales ($k > 0.1$ m^{-1}). We note that the residual is larger for the spectral flux calculation than for the total energy budget (Fig. 11), because the smoothing from the 5-min averaging process artificially reduces the estimate of the explicit dissipation rate.

Large-scale baroclinic waves ($k < 0.01$ m^{-1}) continue to gain kinetic energy from buoyancy production generated through the slumping of the mixed layer front through hour 96 (Figs. 14a,b). At hour 84, large-scale eddy energy is lost through the energy flux divergence term, even though the overall kinetic energy is still increasing (see Fig. 11). As the eddies form closed circulations at hour 96, the energy flux divergence term acts to redistribute kinetic energy upscale as shown by the negative values for $k \sim 0.003$ m^{-1} and positive values for $k \sim 0.002$ m^{-1}. Baroclinic modes clearly dominate the energy balance at large scales while turbulence formation and dissipation at small scales close the budget. There is almost no indication of significant energy production or dissipation at wavenumbers between 10^{-2} and 10^{-1} m^{-1} (Figs. 14a,b). This result could be misinterpreted as an indication that an inertial subrange exists between the baroclinic modes and turbulence at the dissipation scales. However, the physical structure of the flow, with energetic turbulence appearing only at intensified fronts, and the reduced strength of eddies at intermediate scales indicated by the steep spectral slope

(Fig. 13) suggest that turbulence is gaining significant energy primarily through nonlocal spectral transfer rather than through a continuous forward cascade.

The spectral energy budget (8) at turbulence scales (Figs. 14a,b, $k > 0.1$ m^{-1}) shows a peak in energy flux divergence associated with small-scale instabilities in the frontal region (Fig. 4). At these scales, perturbation kinetic energy is lost via negative buoyancy production when vertical mixing destroys stratification associated with the sloping fronts and the mixed layer base. Dissipation is a maximum near the grid scale at about $k = 0.8$ m^{-1}. However, because the spectral decomposition (8) of the energy budget is not fully compatible with the numerical discretization and because the model grid spacing is relatively coarse for simulating turbulent eddies, there is also a fractional residual that is relatively large at these small scales, where the budget terms are all small. The residual in the total kinetic energy budget is negligible (Fig. 11). The flow-dependent turbulence closure in the LES model allows relatively large velocity fluctuations at small scales, with a steep rolloff of the kinetic energy spectrum just above the grid scale (Fig. 13). This evidently exaggerates the incompatibility between the spectral decomposition (8) and the discretization, leading to a larger residual near the grid scale than may be seen in hydrostatic circulation models that spread viscous dissipation over a wider range of larger scales, such as the simulations described by Capet et al. (2008c). Note in this context that a related incompatibility is recognized by Capet et al. (2008c), who argue that their near-zero model shear-production term can be separated ex post facto, by an alternative numerical discretization, into a positive production term and a balancing negative term arising from the model discretization that is presumed to represent a physical dissipation. In any case, our main conclusion is that the transfer of energy from the larger, baroclinic modes to small-scale turbulence is a more direct process that is less dependent on a cascade of energy than would be the case for a classical shear or buoyancy driven turbulent boundary layer.

The overall energy balance can be compared with that presented by Capet et al. (2008c) for their primitive equation simulation of statistically stationary flow in a doubly periodic ocean domain with computational grid resolution on the order of 250 m, roughly two orders of magnitude coarser than the present simulations. The vertical profiles of horizontally averaged kinetic energy terms (Fig. 12) are broadly similar to those presented by Capet et al. (2008c, their Fig. 2b). Capet et al. (2008c) found a $-5/3$ slope in horizontal wavenumber spectra of kinetic energy; however, their analysis of the spectral energy budget indicated that energy flux divergence and dissipation were significant loss terms across much of the spectrum, and they also concluded that the downscale transfer of energy from mesoscale to submesoscale eddies should not be characterized as an inertial subrange. There are basic differences between this study and Capet et al. (2008c): our solutions represent a baroclinic life cycle phenomenon without large-scale forcing, in comparison with their simulations of a fully developed, statistically stationary flow that is in equilibrium with large-scale forcing and has a higher overall energy level. Nevertheless, near $k = 10^{-3}$ m^{-1}, where our study overlaps Capet et al. (2008c), there is an approximate match in the magnitudes of the two sets of spectral energy budget terms.

6. Baroclinic eddy flux

Accurate simulation of frontal instabilities is critical for large-scale oceanographic models. These instabilities help determine both the rate of frontal slumping or lateral restratification and mixing between water masses on each side of the front. Slumping is clearly active in the present idealized case as is evident from comparisons of the meridionally averaged cross sections of temperature at hours 48 and 96 (Fig. 15). The warmer water in the center of the domain spreads laterally, increasing the mixed layer stratification over a broad area and reducing the meridional-mean zonal gradients. As noted in section 4, diapycnal fluxes are weak during the evolution of the frontal instability, so that much of the apparent mixing inferred from these cross sections, especially that near the surface, arises from meridional averaging over small-scale filamentary and eddy structures. The effect of the instabilities can also be analyzed in terms of potential vorticity fluxes (e.g., Samelson and Chapman 1995), but in the present case this approach does not yield substantial new insights; rather, since the potential vorticity field contains higher spatial derivatives of basic flow variables than the temperature field, it is more dominated by small-scale fluctuations whose connection to the frontal-scale evolution is less clear.

Classical estimates of baroclinic eddy fluxes based on linear theory (Green 1970; Stone 1972) suggest that the cross-frontal buoyancy flux $\overline{u'b'}$, where $b' = g\alpha T'$, $T' = T - \overline{T}$, and the overbar denotes a meridional average, should be roughly on the order of $N^2H^2M^2R/f$, where $N^2 = B_z$ is a mean squared buoyancy frequency, H is the disturbance (mixed layer) depth, $M^2 = B_x$ is a mean squared cross-frontal buoyancy gradient, f is the Coriolis parameter, and R is a factor depending on the Richardson number $\mathrm{Ri} = N^2f^2/M^4$ that is near one when Ri is also near one. Using typical values from the simulation of $H = 90$ m, $\partial T'/\partial x = 0.1$ K/2000 m, and $\partial T'/\partial z = 0.1$ K/90 m yields $\mathrm{Ri} = 2$ and a cross-frontal flux estimate

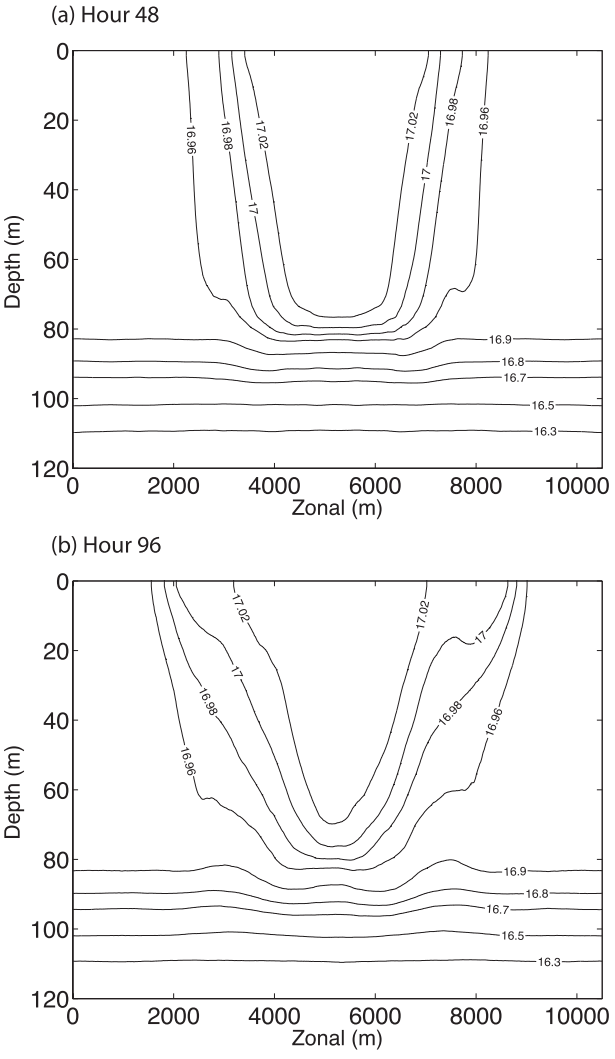

FIG. 15. Meridionally averaged temperature (°C) at hours (a) 48 and (b) 96.

of 2×10^{-5} m^2 s^{-3}. If a proportionality constant on the order of 0.1 is assumed, as in the more detailed flux parameterizations suggested by Fox-Kemper et al. (2008) and Fox-Kemper and Ferrari (2008), then this estimate compares well with an instantaneous, directly calculated flux from the model (Fig. 16). Note that much of the model flux does not represent small-scale mixing but instead arises from reversible, advective displacements of isotherms, which appear as eddy fluxes in the meridional average. Most of this advective transport is accomplished by the large baroclinic waves with closed eddy circulations that have separated from the main frontal region. Actual mixing of the frontal interface has not occurred at hour 96. In fact, continuing this simulation to hour 120 shows that spreading of the front is still limited with most of the small-scale mixing confined to the detached

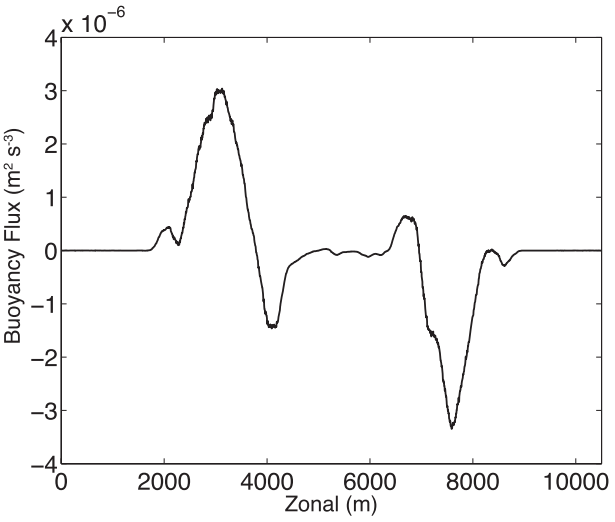

FIG. 16. Meridionally averaged eddy buoyancy flux ($\overline{u'b'}$) at hour 96 from a depth of 13.5 m.

eddies (Fig. 17). More active irreversible mixing over this time scale requires surface forcing, which will be the subject of a future study by the present authors; preliminary analysis indicates that surface forcing can also strongly affect the baroclinic wave processes. Ultimately, the lateral fluxes by baroclinic wave activity will lead to irreversible mixing of lateral gradients via weak turbulence (Figs. 4–6); however, the process requires long periods of time if wind- and wave-forced turbulences are not active.

7. Conclusions

The central goal of this study was to use highly resolved (isotropic 3-m grid) large-eddy simulations on horizontally large (5–10 km) domains to investigate the transfer of energy from baroclinic disturbances of the geostrophic flow to small-scale three-dimensional turbulence, in the absence of wind and wave boundary layer

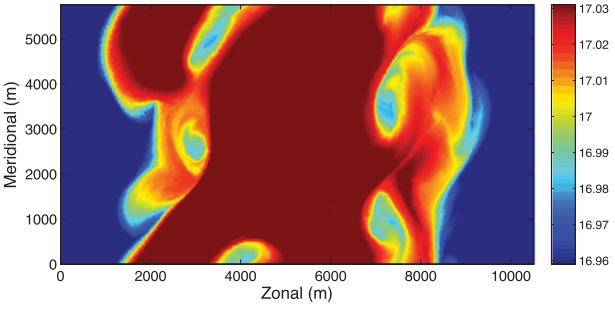

FIG. 17. Horizontal section of temperature (°C) taken at hour 120 from a depth of 4.5 m.

forcing. We find that intense horizontal and vertical shear generated in narrow, highly localized frontal zones can support the development of weak three-dimensional turbulence features that are directly linked to the larger-scale baroclinic waves. The link between the baroclinic eddies and the small-scale turbulence is the development of coherent, anisotropic frontal features through frontogenetic forcing from the large-scale eddies, a process that is strongly nonlocal in wavenumber space.

Based on these results, we conclude that a direct downscale transfer of energy can occur, with elevated turbulence levels and associated irreversible turbulent fluxes arising in certain locations from baroclinic wave activity, but also that a forward energy cascade, defined as a continuous transfer of energy through a broad, scale-invariant, inertial range of wavenumbers, does not exist, at least in these limited-duration simulations. The essentially laminar collapse of the large-scale gradients to the localized frontal scale, followed by the local onset of turbulent overturning, results in a direct, spectrally nonlocal transfer of energy from the larger-scale baroclinic eddies to small-scale, three-dimensional turbulence, with associated weak enhancements of parameterized irreversible turbulent heat fluxes and kinetic energy dissipation.

The simulations analyzed here represent a baroclinic life cycle phenomenon rather than a continuously forced, statistical equilibrium setting. It is possible that simulations in a statistically stationary configuration would produce a different result. However, the adjustment times of the small-scale turbulence are much shorter than those of the larger-scale field; consequently, the levels of small-scale turbulence are likely to be reasonably well simulated in the present setting, relative to the level of baroclinic wave activity. It seems unlikely that equilibrium simulations would yield essentially different results unless baroclinic wave characteristics in the present case are significantly different from wave behavior in an equilibrium configuration. Our initialization of a vertically aligned front having negative potential vorticity might also indicate that symmetric instability could be active as part of the small-scale destabilization process. However, simulations with sloped fronts having initially positive potential vorticity displayed a similar behavior with three-dimensional turbulence concentrated along frontal boundaries without a banded structure aligned with the front as might be expected with symmetric instability (e.g., Taylor and Ferrari 2009).

The present simulations have been conducted for a shallow domain representative of the ocean surface boundary layer. However, no wind or wave surface boundary layer forcing was introduced. As may be anticipated from the extremely low levels of turbulent activity in the present simulations, preliminary simulations with wind and wave forcing show significantly different turbulent and irreversible mixing responses, which have a substantial impact on the baroclinic wave development.

Acknowledgments. This research was funded by the Office of Naval Research Grant N00014-09-1-0268. Supercomputer resources were provided through the Department of Defense High Performance Computer Modernization Program.

REFERENCES

Boccaletti, G., R. Ferrari, and B. Fox-Kemper, 2007: Mixed layer instabilities and restratification. *J. Phys. Oceanogr.,* **37,** 2228–2250.

Capet, X., J. C. McWilliams, M. J. Molemaker, and A. F. Shchepetkin, 2008a: Mesoscale to submesoscale transition in the California Current System. Part I: Flow structure, eddy flux, and observational tests. *J. Phys. Oceanogr.,* **38,** 29–43.

——, ——, ——, and ——, 2008b: Mesoscale to submesoscale transition in the California Current System. Part II: Frontal processes. *J. Phys. Oceanogr.,* **38,** 44–64.

——, ——, ——, and ——, 2008c: Mesoscale to submesoscale transition in the California Current System. Part III: Energy balance and flux. *J. Phys. Oceanogr.,* **38,** 2256–2269.

Charney, J. G., 1971: Geostrophic turbulence. *J. Atmos. Sci.,* **28,** 1087–1095.

Ducros, F., P. Comte, and M. Lesieur, 1996: Large-eddy simulation of transition to turbulence in a boundary layer developing spatially over a flat plate. *J. Fluid Mech.,* **326,** 1–36.

Fox-Kemper, B., and R. Ferrari, 2008: Parameterization of mixed layer eddies. Part II: Prognosis and impact. *J. Phys. Oceanogr.,* **38,** 1166–1179.

——, ——, and R. Hallberg, 2008: Parameterization of mixed layer eddies. Part I: Theory and diagnosis. *J. Phys. Oceanogr.,* **38,** 1145–1165.

Frisch, U., 1995: *Turbulence.* Cambridge University Press, 296 pp.

Green, J. S., 1970: Transfer properties of the large-scale eddies and the general circulation of the atmosphere. *Quart. J. Roy. Meteor. Soc.,* **96,** 157–185.

Henyey, F. S., J. Wright, and S. M. Flatté, 1986: Energy and action flow through the internal wave field: An Eikonal approach. *J. Geophys. Res.,* **91** (C7), 8487–8495.

Hoskins, J. B., and F. P. Bretherton, 1972: Atmospheric frontogenesis models: Mathematical formulation and solution. *J. Atmos. Sci.,* **29,** 11–37.

Molemaker, M. J., J. C. McWilliams, and X. Capet, 2010: Balanced and unbalanced routes to dissipation in an equilibrated Eady flow. *J. Fluid Mech.,* **654,** 35–63.

Rhines, P. B., 1977: The dynamics of unsteady currents. *The Sea,* E. A. Goldberg, Ed., *Marine Modeling,* Vol. 6, John Wiley and Sons, 189–318.

——, 1979: Geostrophic turbulence. *Annu. Rev. Fluid Mech.,* **11,** 401–441.

Samelson, R. M., 1993: Linear instability of a mixed-layer front. *J. Geophys. Res.,* **98** (C6), 10 195–10 204.

——, and D. C. Chapman, 1995: Evolution of the instability of a mixed-layer front. *J. Geophys. Res.,* **100** (C4), 6743–6759.

Simmons, A. J., and B. J. Hoskins, 1978: Barotropic influences on the growth and decay of some non-linear baroclinic waves. *J. Atmos. Sci.,* **37,** 1679–1684.

Skyllingstad, E. D., W. D. Smyth, and G. B. Crawford, 2000: Resonant wind-driven mixing in the ocean boundary layer. *J. Phys. Oceanogr.,* **30,** 1866–1890.

Smolarkiewicz, P. K., and L. G. Margolin, 1994: Variational solver for elliptical problems in atmospheric flows. *Appl. Math. Comput. Sci.,* **4,** 527–551.

Stone, P. H., 1966: On non-geostrophic baroclinic stability. *J. Phys. Oceanogr.,* **23,** 390–400.

——, 1972: A simplified radiative-dynamical model for the static stability of rotating atmospheres. *J. Atmos. Sci.,* **29,** 405–418.

Taylor, J. R., and R. Ferrari, 2009: On the equilibration of a symmetrically unstable front via a secondary shear instability. *J. Fluid Mech.,* **622,** 103–113.

Tennekes, H., and J. Lumley, 1972: *A First Course in Turbulence*. MIT Press, 300 pp.

Thorpe, S. A., 2004: Langmuir circulation. *Annu. Rev. Fluid Mech.,* **36,** 55–79.